



# The Examination of Microstructure and Thermal Oxidation Behavior of Laser-Remelted High-Velocity Oxygen Liquid Fuel Fe/Al Coating

Kadir Mert Doleker

(Submitted March 9, 2020; in revised form May 14, 2020; published online June 8, 2020)

Aluminide intermetallics with superior mechanical and thermal properties can be produced using various techniques. Laser-remelted coating surfaces provide lower porosity and superior adhesion to the substrate. In the present study, Fe and Al powders were sprayed on the 316L stainless steel substrate using high-velocity oxygen liquid fuel (HVOLF) technique. The produced composite coating was subjected to laser heat treatment for the remelting of the coating layer. HVOLF Fe/Al coating, the remelted coating and the substrate were exposed to isothermal oxidation tests at 950 °C for 5, 25, 50 and 100 h. Before and after the oxidation tests, the samples were characterized using x-ray diffraction, scanning electron microscopy (SEM) and SEM elemental mapping analysis. Fe and Al were alloyed with the substrate via laser melting, and thus, an alumina-forming surface layer was obtained. Besides, the surface hardness of the substrate was increased by the remelting process. After the oxidation tests, the obtained results showed that the laser-remelted coating exhibits better oxidation performance compared to the substrate material and HVOLF Fe/Al coating with the effect of the formation of the protective alumina oxide layer.

**Keywords** Fe/Al composite, FeAl, HVOLF, intermetallic, oxidation, remelting

## 1. Introduction

Thermal spray coatings are widely used in machine components to prolong their lifetime. Thermal spray family involves many methods such as plasma spray (PS), high-velocity oxygen fuel (HVOF), flame spray and electric arc spray (Ref 1-3). HVOF is a very popular technique for metallic powder deposition in the thermal spray family. Recently, liquid fuel has started to be used instead of gaseous fuel to increase the quality of coatings. The usage of liquid fuel in HVOF technique provides higher kinetic energy and a denser coating structure (Ref 4, 5). Denser coating structures are desired in high-temperature conditions as porosity and gaps in the structure act as internal oxygen reservoirs. In HVOF deposition technique, there are many process parameters for improving the coating microstructure such as feedstock powders, fuel type, the oxygen–fuel gas ratio, the carrier gas, gun design and distance. Sprayed powders' velocity and their in-flight particle temperature can be improved by changing these parameters. Cabral-Miramontes et al. (Ref 6) investigated the distance parameter's effect on HVOF CoNiCrAlY coatings. They determined that modifying the distance between the gun and the substrate affected some properties such as oxides, porosity, unmelted particles and contamination in the coatings' microstructure. Song et al. (Ref 7) compared the oxidation

performance of HVOLF NiCr coating by changing the ratio of oxygen/fuel stoichiometry. The altered parameters affected the oxidation performance of NiCr coatings due to the variation in the porosity and oxide content. As the microstructural properties alter depending on the spraying parameters, the oxidation performance of coatings also changes. In the production of a high-quality coating, parameter optimization requires good experience and time. From this perspective, other techniques may be tried to improve coating properties as well. In order to improve the coating structure, the remelting process may be applied on coating surfaces using flame, furnace, electron beam or laser beam (Ref 8-12). Laser surface remelting can be widely used for improvement of materials' surface properties such as microstructure, homogenization, repairing of cracks or densification of the coating layer (Ref 13-15). In particular, microstructural properties, defects and corrosion resistance in metal matrix composite (MMC) coatings can be modified by the usage of laser treatments (Ref 16). Splats forming during thermal spraying can be removed by remelting or partially remelting effect. Similarly, porosity or discontinuous openings can be decreased fully or partially.

High-temperature oxidation is a very destructive degradation mechanism for metallic parts. At elevated temperatures, if metallic material does not form a protective oxide layer on its surface, it loses too much base mass. Unstable and fast-growing oxides do not provide a protective effect to the base metal. Fast-growing oxides generally break down very quickly and show rapid growth. After they are spalled from the base metal, they grow again rapidly. Aluminide coatings provide a protective oxide scale under oxidizing ambients. FeAl intermetallic has low cost and low density. It can be used in high-temperature applications due to its high corrosion resistance, high melting point and high creep resistance (Ref 17). Fe-Al intermetallics form stable aluminum oxide ( $\alpha$ -Al<sub>2</sub>O<sub>3</sub>) on their surfaces by selective oxidation of aluminum, which has a positive contribution to oxidation and corrosion behaviors at high tempera-

Kadir Mert Doleker, Engineering Faculty, Metallurgical and Materials Engineering, Ondokuz Mayıs University, Kurupelit Campus, Samsun, Turkey. Contact e-mail: mertdoleker@gmail.com.

tures (Ref 18). The formation of the alumina layer on the surface of metal provides a good barrier against oxygen penetration, and thus, the formation of other faster-grown oxides is retarded.

In the present study, the main purpose is to improve the high-temperature oxidation resistance of 316 L stainless steel using coating and remelting processes. 316 L stainless steel substrate was firstly coated with composite Fe/Al powders, and secondly, coated surfaces were remelted by laser to form an aluminum-containing alloy. Fe and Al powders were not subjected to the powder preparation processes such as gas atomization or mechanical alloying. In addition, the parameters of HVOLF spraying were not optimized. With the laser melting process, such negativities were eliminated and a dense coating structure was obtained quickly and practically. The substrate, HVOLF Fe/Al coating and remelted Fe/Al coating were subjected to isothermal oxidation tests in order to compare their oxidation resistance.

## 2. Experimental Study

Commercially available AISI 316L stainless steel material was used as the substrate material. The chemical composition of 316L stainless steel is shown in Table 1. The substrate material is rich in Fe, Cr and Ni elements.

The substrate material was grit-blasted using alumina particles ( $40 \pm 5 \mu\text{m}$ , 2.5 bar) before HVOLF coating process. Fe (50% at., Nanokar, 120  $\mu\text{m}$ ) and Al (50% at., Nanokar, 100  $\mu\text{m}$ ) with 99.9% purity powders were mechanically mixed for 2 h. The mixed powders were sprayed on a substrate using HVOLF (Oerlikon Metco WokaStar-610-Sz) technique. HVOLF coating process parameters are shown in Table 2.

Fe/Al-coated substrate was subjected to the laser remelting process (Alpha laser, AL-300). Laser remelting parameters are given in Table 3.

Isothermal high-temperature oxidation tests were carried out on the substrate, Fe/Al coating and the remelted coating at 950 °C for 5, 25, 50 and 100 h using the electric furnace (Protherm PLF 130/12) in the ambient atmosphere. The graphical illustration of the experimental procedure is presented in Fig. 1.

XRD analysis (Rigaku, Cu-K $\alpha$  radiation) was performed on the samples before and after the oxidation tests for the phase characterization. In addition, the microstructures of the samples were examined with SEM (Tescan MAIA3) and EDS mapping analysis. Oxide layer thickness belonging to the oxidized samples was measured using Image Pro Plus 6 software program. Ten measurements taken from five SEM-BSE (backscattered electron) images were used for the calculation of the average oxide thickness. Porosity measurement was taken using Image J software program. Similar to oxide thickness, ten measurements taken from five SEM-BSE images

**Table 1 Chemical composition of commercially available AISI 316L stainless steel**

Fe	Cr	Ni	Mo	Mn	Si	C	P	S
Balance	16-18	10-14	2-3	2	1	0.03	0.045	0.03

were used in the calculation of the porosity content's percentage. The hardness measurement depending on the distance from the surface was taken under 100 g load and 15 s using Vickers Microhardness Tester (Qness, Q10).

## 3. Results and Discussion

### 3.1 The Characterization of as-Sprayed and as-Remelted Fe/Al Coating

The cross-sectional SEM and elemental mapping images belonging to the as-sprayed Fe/Al composite coatings are shown in Fig. 2. As shown in the figure, the coating thickness is about 250  $\mu\text{m}$ . The Fe/Al composite coating has a uniform microstructure as shown in Fig. 2. The elemental distributions by weight of Fe and Al are close to each other in the coated structure. This can be understood from the spectrum data. While dark colors represent Al, gray colors belong to Fe elements. It is seen that there is almost equal elemental distribution. The coating also contains a small amount of porosity and oxide based on the production technique. The porosity content of the coating was measured as 1.8% according to the cross-sectional SEM image analysis results. This may be a high value for HVOLF coating technique due to the non-optimized coating parameter. Chmielewski et al. (Ref 19) produced a Fe/Al composite coating using an arc spray technique. According to their SEM and optical microscopy images, the coating structure has higher oxide and porosity compared to this study due to their production technique.

Figure 3 shows the SEM microstructure, elemental line and point analyses of the laser melted zone and the substrate belonging to the laser-remelted coating. After the laser melting process, coating porosity significantly decreased and the coating layer adhered in a more compact form on the substrate. The elemental line analysis and the contrast difference in the SEM image show the interface of the substrate and the laser-remelted zone. The laser-remelted zone is slightly darker than the substrate due to the elemental contrast difference. According to the elemental line analysis, the remelted layer has higher Al and Fe concentration and lower Ni and Cr concentration as compared to the substrate. The elemental distribution (wt.%) of the coating changed significantly due to the diffusion of the elements between the substrate and the coating. According to Fig. 3, Al slightly oxidized and vaporized during the laser process and thus decreased as compared to Fe, Ni and Cr concentration. The interdiffusion zone (IDZ) is not visible in the SEM image, yet it can be detected by elemental line analysis. In this region, which has a thickness of about 30  $\mu\text{m}$ , elemental concentration change is observed. The formation of a thin alumina layer is shown in Fig. 3. This also provides an advantage against oxidation prior to oxidation tests.

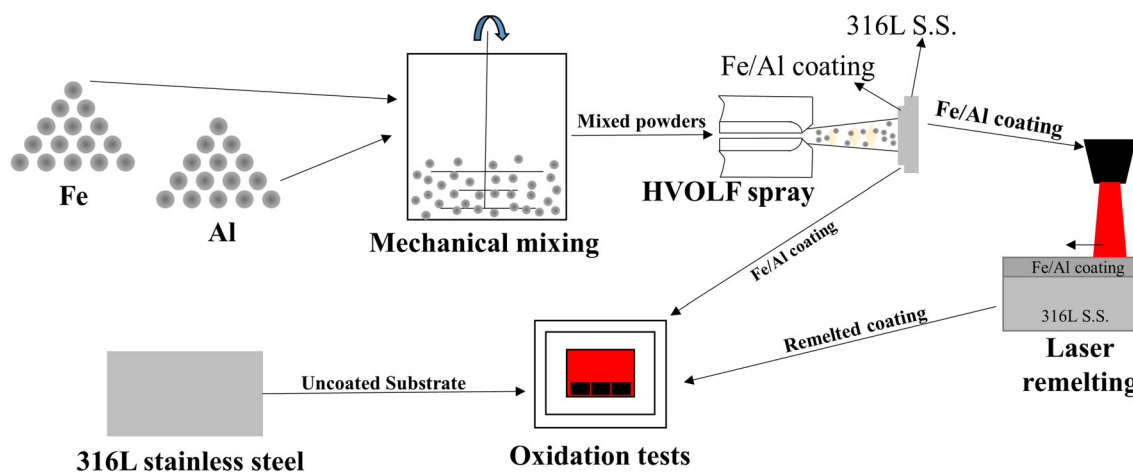
In the literature (Ref 20, 21), powder mixtures of Ni and Al were sprayed on a substrate using cold spray technique after the ball milling process. The produced coatings were subjected to post-treatment for the formation of intermetallic phases, and local Ni-Al intermetallic phase formations were achieved. Wang et al. (Ref 22) studied the effect of heat treatment on the formation of FeAl intermetallic phase in the cold sprayed iron/aluminum composite coating. FeAl intermetallic phases were formed at 900 °C, while Fe, Al and Fe<sub>2</sub>Al<sub>5</sub> phases were detected at 600 and 700 °C. With increasing temperature, the

**Table 2 HVOLF spray parameter of Fe/Al coating**

Powder carrier gas, N	Fuel (kerosene) flow rate	O <sub>2</sub> flow rate	Distance	Gun speed
5, l/min	1.89, l/h	800, l/min	250, mm	10, mm/s

**Table 3 Laser melting parameter of Fe/Al coating**

Laser power	Pulse frequency	Pulse duration	Spot diameter	Scanning rate	CO <sub>2</sub> flow rate
212, W	16, Hz	6, ms	1, mm	2.8, mm/min	10, l/min

**Fig. 1** Graphical abstract of the experimental procedure

proportion of intermetallic phases increased as the liquid aluminum surrounded more iron. Instead of these processes, aluminum-containing alloy formation was achieved by laser remelting process. Similar to this study (Ref 23), Al was deposited on the steel substrate using thermal spray technique, and then, the remelting process by CO<sub>2</sub> laser beam was applied on the Al-coated steel. FeAl, Al<sub>2</sub>O<sub>3</sub> and FeSi<sub>2</sub> phases were detected by XRD after the remelting process. In our study, Fe/Al-coated layer causes the formation of Fe<sub>3</sub>Al intermetallic phase with a lower Al content after the laser remelting process. Similarly, Al<sub>2</sub>O<sub>3</sub> phase formation was detected in this study.

Before and after the remelting process, the variation of hardness depending on the distance from the surface is shown in Fig. 4. The hardness values of Fe/Al coating are lower than both the substrate and the remelted coating due to free Al and Fe particles. Chmielewski et al. (Ref 19) obtained 230–265 Hv values after arc spray Fe/Al coating. This may be related to the low speed of the spraying process enabling higher alloying effect between Al and Fe particles. In this study, the as-sprayed coating structure does not include local intermetallic formations and it is not rich in oxide by contrast with their study. Thus, the hardness of as-sprayed coating value is lower in this study. After the remelting process, the substrate and Fe/Al particles were alloyed with the effect of laser melting. The hardness values of the remelted layer increased about threefold compared to Fe/Al coating. It is thought that the increase in the remelted coating is related to the distortion of the  $\gamma$  lattice due to the high atomic radii of Al compared to the other elements in the lattice

and also the formation of Fe<sub>3</sub>Al intermetallic phases. The hardness values do not show a significant change until the interdiffusion zone (IDZ). The hardness value of IDZ decreased by about twofold compared to the remelted layer.

### 3.2 High-Temperature Oxidation Behavior of 316L Stainless Steel

The XRD patterns belonging to 316L stainless steel before and after 50-h oxidation tests are shown in Fig. 5. The oxide phases are Cr<sub>2</sub>O<sub>3</sub>, Fe<sub>2</sub>O<sub>3</sub>, Fe<sub>3</sub>O<sub>4</sub> and spinel (Fe, Ni)Cr<sub>2</sub>O<sub>4</sub>. The substrate includes enough Cr content for the formation of a protective Cr<sub>2</sub>O<sub>3</sub> layer. However, Cr<sub>2</sub>O<sub>3</sub> did not provide a good barrier against oxidation due to the effect of high temperature and long oxidation period. The XRD analysis result shows that the cations of other elements except for Cr diffused outwards and reacted with oxygen and the oxide layer. As a result, chromium oxide, iron oxides and spinel oxides are formed on the surface.

In Fig. 6, cross-sectional SEM images and elemental mapping analysis results of the substrate material after 25-h and 50-h oxidized are shown. After the 5-h isothermal oxidation test, micro-cracks and a thick oxide layer (23.5  $\mu$ m) can be observed in the SEM image. Cracks were formed on the upper layer of the formed oxide layer, while there was no crack formation at the interface between the substrate and the oxide layer. The oxide thickness increased with increasing oxidation period and reached 33  $\mu$ m at the end of the 25-h oxidation test. Interestingly, no crack formation was observed in the oxide

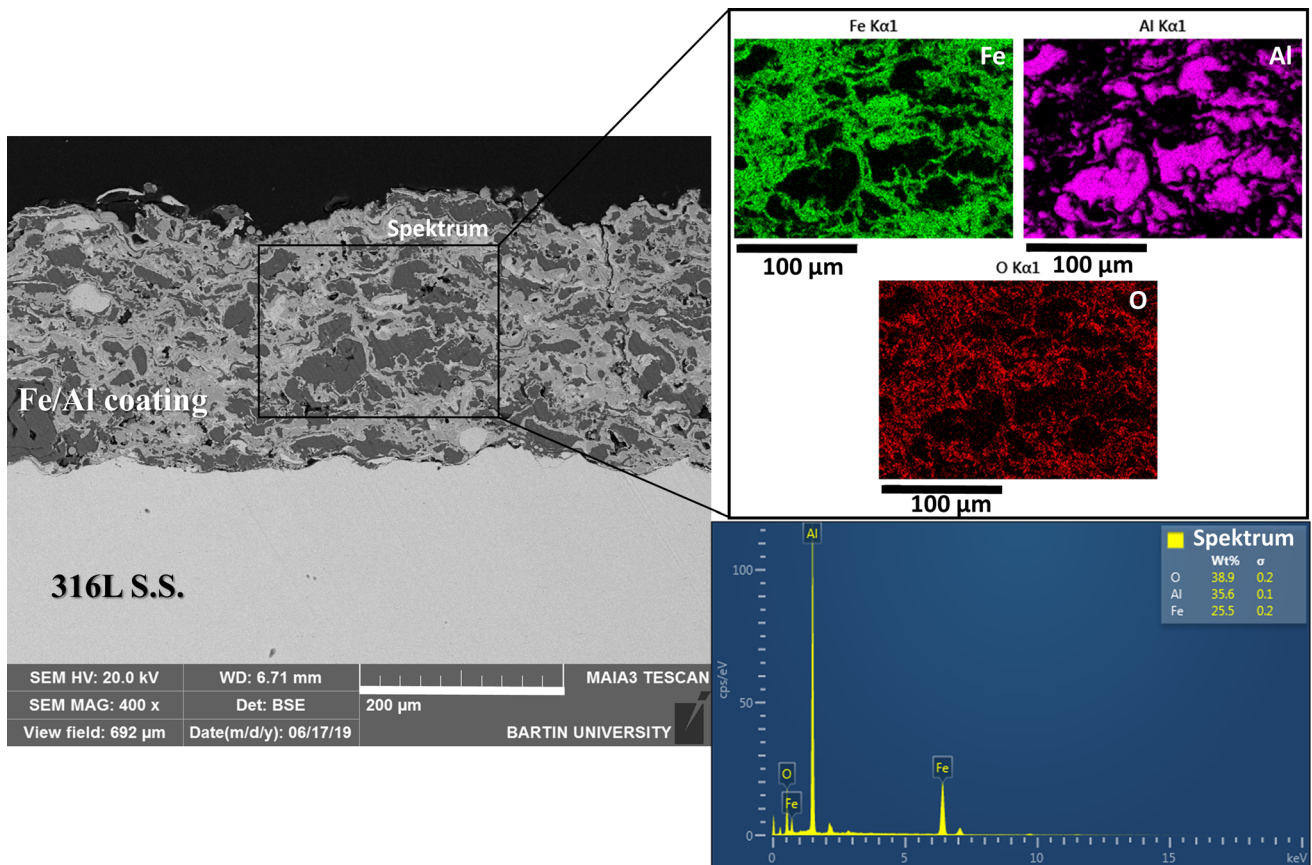


**Fig. 2** SEM and elemental mapping images of as-sprayed HVOLF Fe/Al coating

layer. After the oxidation tests, many oxide layers belonging to the substrate include cracks on the top oxide layer. This is related to the low fracture toughness of iron oxide. However, the oxide layer in 25-h oxidized sample does not include crack formation, interestingly. This situation is also related to the non-homogeneous oxide growth in the substrate material. In 50-h oxidation test, the oxide layer begins to crack, completely. Especially during the cooling, thermal stresses caused the cracking of the oxide layer from the interface. After the 100-h oxidation test, the oxide layer completely spalled from the substrate. In fact, the oxide layer started to separate from the substrate after 50-h oxidation. A new oxide layer formed on the substrate with the increased oxidation time. According to the elemental distribution results, the formed oxide layer composed of Fe, Ni and Cr-based oxides. It is estimated in terms of coincided elements that while  $\text{Cr}_2\text{O}_3$  formed predominantly in the inner oxide layers,  $(\text{Fe, Ni})\text{Cr}_2\text{O}_4$  spinel phases occurred in the middle layer and  $\text{Fe}_2\text{O}_3$  phases occurred in the upper regions of the oxide layer until 50-h oxidation test. At the end of 50-h oxidation test, the oxide thickness layer is about 42 µm and the oxide layer included cracks at the interface. The elemental distribution of the oxide layer is similar to the formed oxide layer at the end of the 25-h oxidation test. The oxide layer spalled from the spinel oxide layer after 100-h oxidation. The separated oxide layer consists of  $\text{Fe}_2\text{O}_3$ , while the inner oxide layer comprises  $(\text{Fe, Ni})\text{Cr}_2\text{O}_4$  and  $\text{Cr}_2\text{O}_3$ . This failure is probably related to the thermal expansion mismatch and low fracture toughness between the oxide layers. Both  $\text{Fe}_2\text{O}_3$  and spinel oxides have a high growth rate and low toughness. In addition, these types of oxides include structures with pores

during high-temperature oxidation. These pores can be seen on  $\text{Fe}_2\text{O}_3$  layer in the SEM image belonging to 100-h oxidation. It can be understood that both obtained oxide scales ( $\text{Fe}_2\text{O}_3$  and spinel) almost grow with equal ratio during the oxidation period. The increased oxidation time causes higher stress in the coating layer. Thus, delamination occurs inevitably at the end of the oxidation test. It can be said that the breakaway oxidation regime started after 50 h. The obtained results show that the formed oxide layer and its growth behavior are not stable and suitable for oxidation at 950 °C. However, Buscail et al. (Ref 24) studied the isothermal oxidation behavior of 316 L stainless steel between 800, 900 and 1000 °C for 96 in ambient air. Oxide scale phases were found to be  $\text{Mn}_{1.5}\text{Cr}_{1.5}\text{O}_4$  and  $\text{Cr}_2\text{O}_3$ , while  $\text{SiO}_2$  was also observed as an internal oxide according to the SEM images and EDX analysis. Therefore, the obtained oxide scale thickness is lower than this study.  $\text{FeCr}_2\text{O}_4$  and iron oxide phases grow with higher rates compared to the  $\text{Cr}_2\text{O}_3$  phase. In the present study, despite the presence of Cr in the matrix, other unstable oxides formed on the surface, and thus, higher oxide thickness was obtained.

Figure 7 shows the XRD pattern of Fe/Al coating after 50-h oxidation. The XRD pattern of 100-h oxidized Fe/Al coating is not included in Fig. 7 due to the complete spallation of the coating layer from the substrate. The as-sprayed coating during the deposition was oxidized a little; thus, it includes free Al and Fe phases as well as their oxides in XRD pattern. After the 50-h oxidation period, the coating layer almost completely oxidized and it predominantly consists of  $\text{Fe}_2\text{O}_3$ . This is probably related to early oxidation of Al in the coating layer.

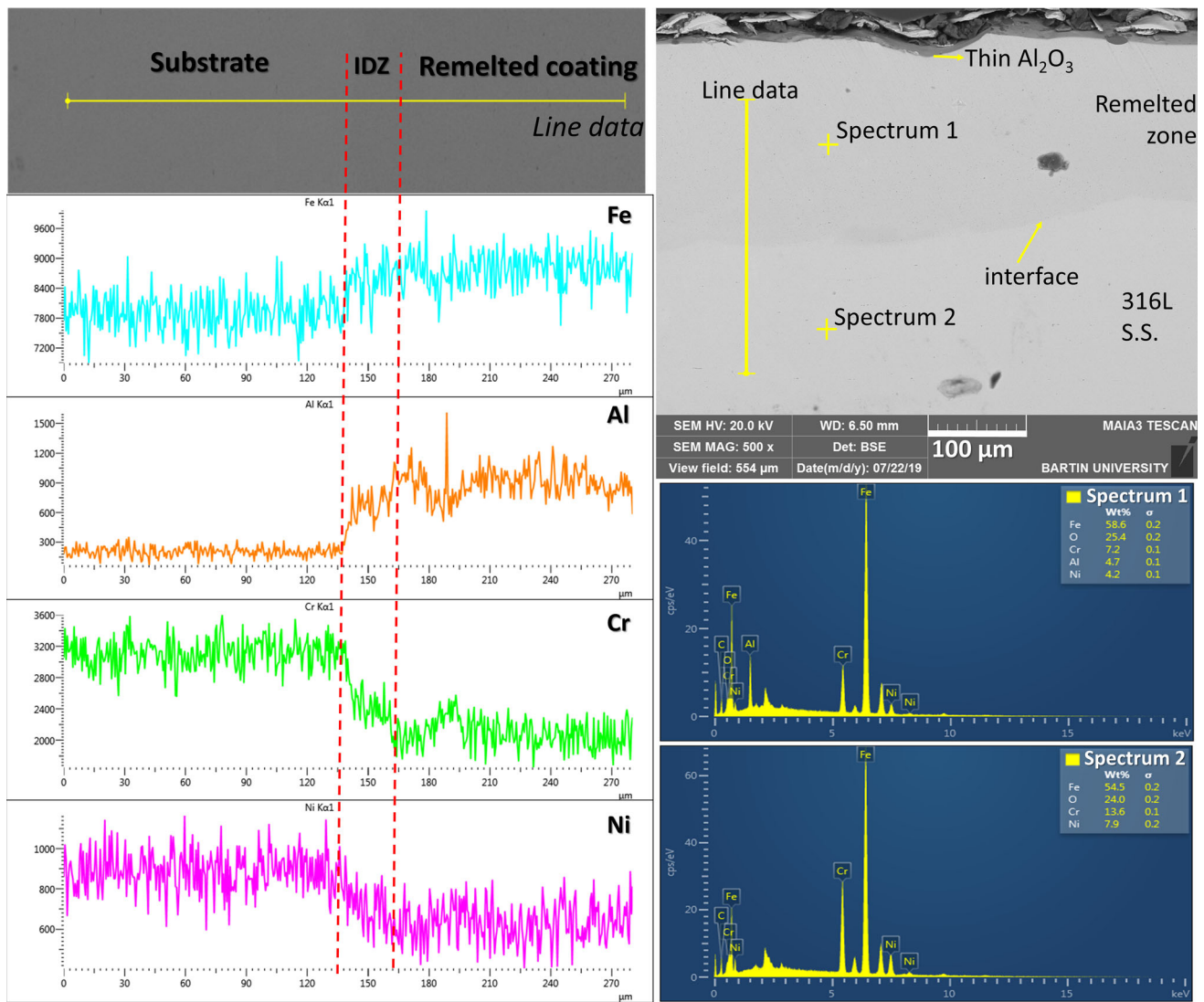


**Fig. 3** SEM and EDS analysis of as-melted HVOLF Fe/Al coating

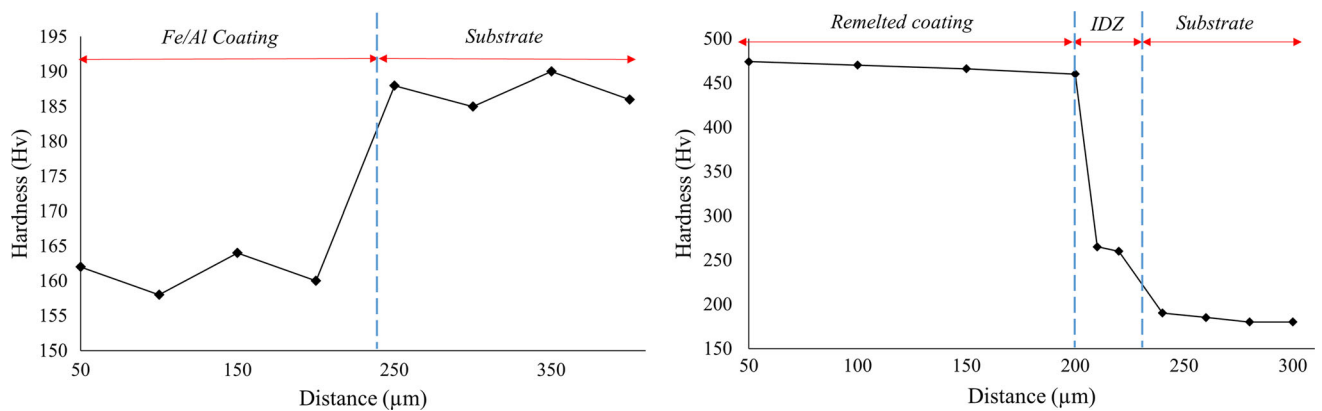


**Fig. 4** Variation of hardness depending on the distance from the surface in Fe/Al coating and remelted coating

Figure 8 shows the SEM and elemental mapping analysis images of Fe/Al coatings after the oxidation tests. In the first stage, there was no crack or separation in the coating layer. However, Fe/Al coating was completely oxidized due to free Fe and Al. After 25-h oxidation, the coating layer was not

separated from the substrate, but it has started to spall. Besides, inner oxidized regions can be seen in the substrate. After the 50-h oxidation test, the coating layer starts to crack from a few regions as well as the interface due to the thermal expansion mismatch and thermal stress. In 100-h oxidation period,

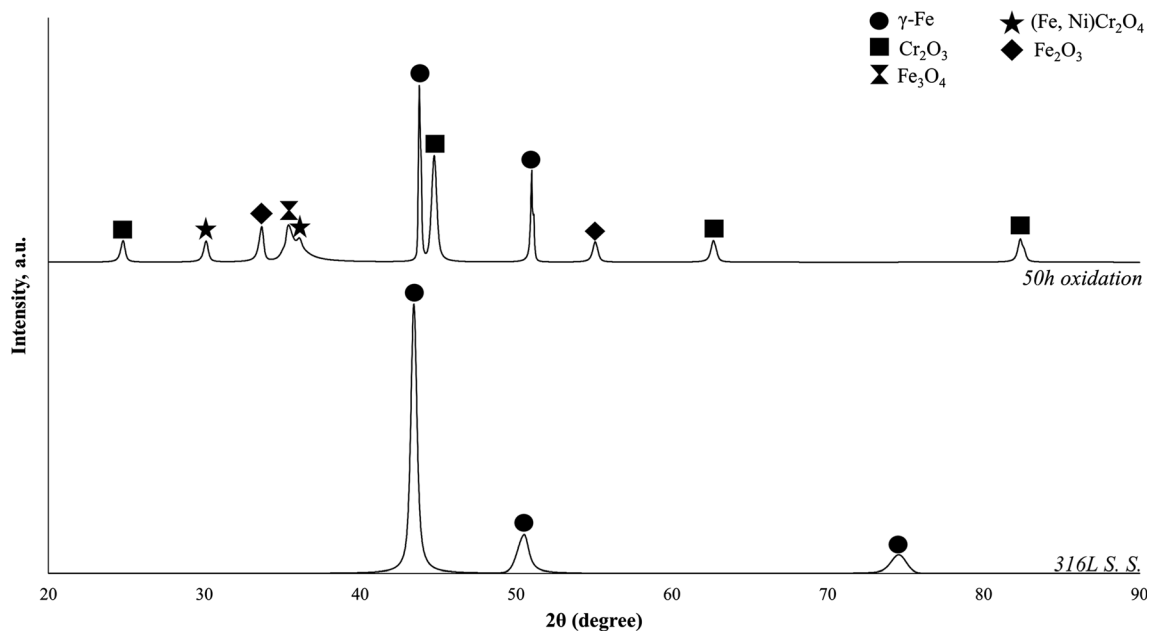


**Fig. 5** XRD patterns of as-received and 50-h oxidized substrate material

sintering effect can be seen in the coating layer. The coating layer completely spalled from the interface between the substrate and the coating layer. This failure is especially related to oxidation of free Fe and Al during the oxidation test. The coating layer has become a ceramic coating layer rather than metallic. Therefore, the important properties such as fracture toughness and thermal expansion decreased and crack formations occurred. The remelting process before the oxidation tests allowed the free Fe and Al to be alloyed with the substrate.

### 3.3 High-Temperature Oxidation Behavior of Laser-Remelted Fe/Al Coating

XRD analysis results of as-remelted, 25- and 50-h oxidized remelted Fe/Al coatings are shown in Fig. 9. The remelted coating is composed of  $\gamma$ -Fe and  $\text{Fe}_3\text{Al}$  as well as  $\text{Al}_2\text{O}_3$ . Alumina formation was observed due to  $\text{CO}_2$  gas usage during the remelting process. The formation of the alumina phase is an advantage due to the oxygen barrier effect prior to the high-temperature oxidation test. This formation may have occurred by the reaction of  $\text{CO}_2$  and Al. Additionally, Al oxidized at relatively lower partial oxygen pressures and probably oxidized slightly during the remelting process which is applied at high temperatures. After the 25-h oxidation test,  $\text{Fe}_3\text{Al}$ ,  $\text{Al}_2\text{O}_3$  and  $\text{Cr}_2\text{O}_3$  phases were detected according to the XRD analysis.  $\text{Fe}_3\text{Al}$  is the dominant phase instead of  $\gamma$ -Fe with the effect of high temperature, while alumina and chromia oxide phases formed at the end of the 25-h oxidation test. Chromia phase may have remained from the initial oxidation stage. After the 50-h oxidation test, matrix phases composed of  $\text{Fe}_3\text{Al}$  and  $\gamma$ -Fe similar to the 25-h oxidation test as the formed oxide phases only consist of alumina. In 100-h oxidation test,  $\text{Fe}_3\text{Al}$  is the matrix phase, while the alumina is the main oxide phase according to the XRD analysis result. No other oxide formation was observed except alumina.

Figure 10 shows the SEM images and elemental mapping analysis results belonging to the laser-remelted coating after 5-, 25-, 50- and 100-h oxidation tests at 950 °C. The obtained

SEM and elemental mapping results show that the formed oxide phase only consists of alumina. Oxide layer thickness increased depending on time. After the 50-h oxidation test, the increase in oxide thickness decreased further. Aluminum presence can be seen in the substrate at the first stage, while it is not visible on the substrate after the 5-h oxidation periods. The formed alumina layer is compact and does not include cracks for each oxidized sample. The oxidized samples do not include an apparent inner oxide formation. In the oxidized samples, no oxide traces are observed except for alumina up to 50 h. However, local small oxide traces can be seen in 100-h oxidized sample. The formation of other oxides may be related to the depletion of Al in the sub-layers.

The SEM image and the elemental analysis results of the interface between the laser melted zone and the substrate after 100-h oxidation are given in Fig. 11. After the oxidation tests, IDZ thickness is increased by about twofold with the effect of high temperature. Al-rich phases (small dark gray colors) can be seen in the remelted zone. In IDZ, Mo and Si can be seen although there is no visible distribution in IDZ according to spectrum 2. These elements are not obtained in the substrate according to spectrum 4. Before the oxidation, N is not visible at the interface yet it coincided with Al after 100-h oxidation. This indicates the formation of AlN phases with the reaction between Al and N in IDZ after the oxidation tests. This is clearly observed in the mapping images and elemental spectrum 3 analysis. Similar phase formation was obtained by Liu et al. (Ref 25). In short oxidation time, they detected pure Al formation in IDZ between Ni-based superalloy and NiCrAlY coating after 5- and 10-h oxidation at 1100 °C. After 25-h oxidation, they detected AlN and TiN phase formations in IDZ. Their suggestion about this formation is that N penetrates the coating by the consumption of O with the effect of oxidation and reacts with solid-soluted Al. This statement is also acceptable for the current study. This formation causes the early depletion of Al-rich phases. However, it did not show a detrimental effect on the oxidation behavior of the laser melted coating.

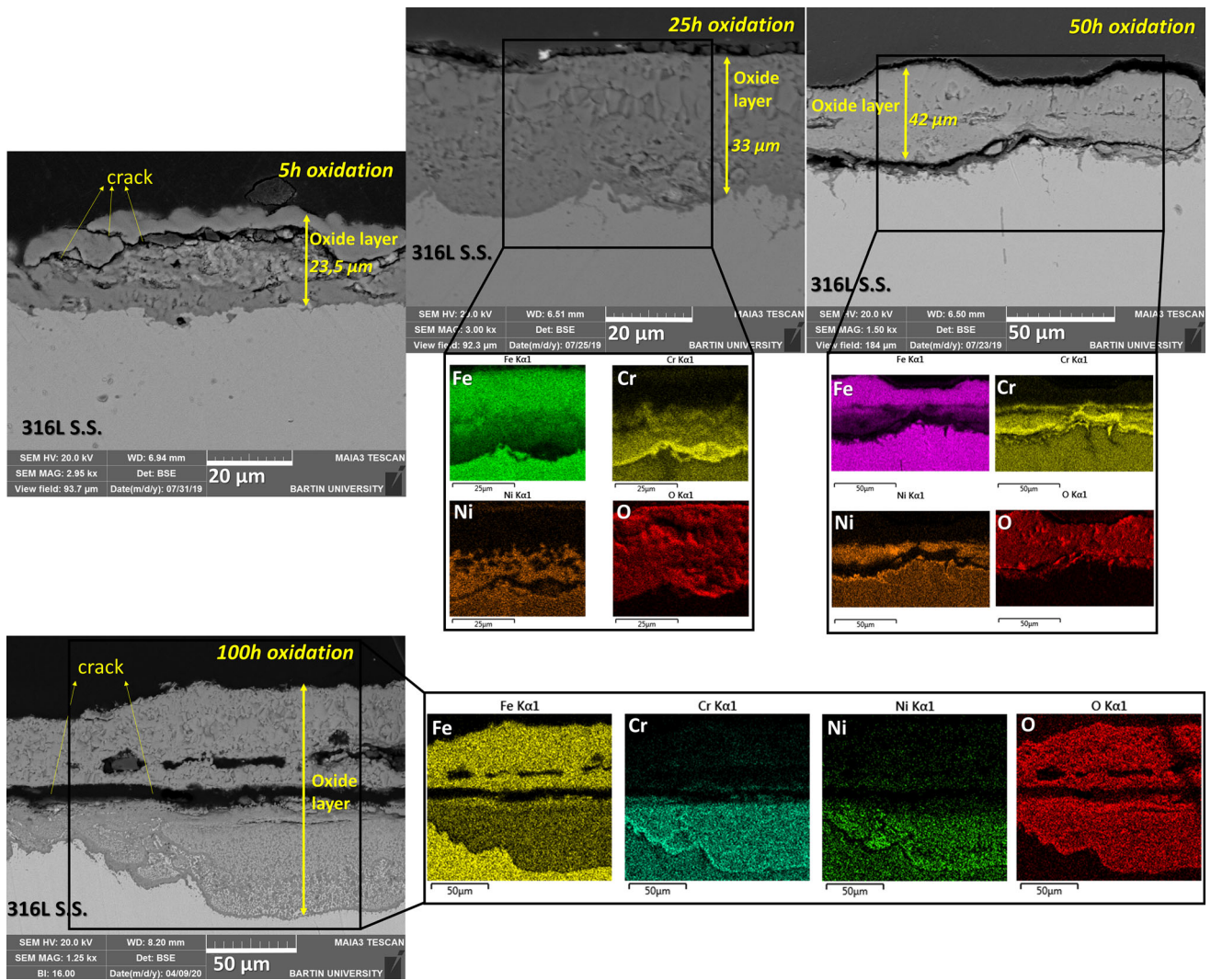


Fig. 6 SEM images of 5-, 25-, 50- and 100-h oxidized 316L stainless steel substrate material

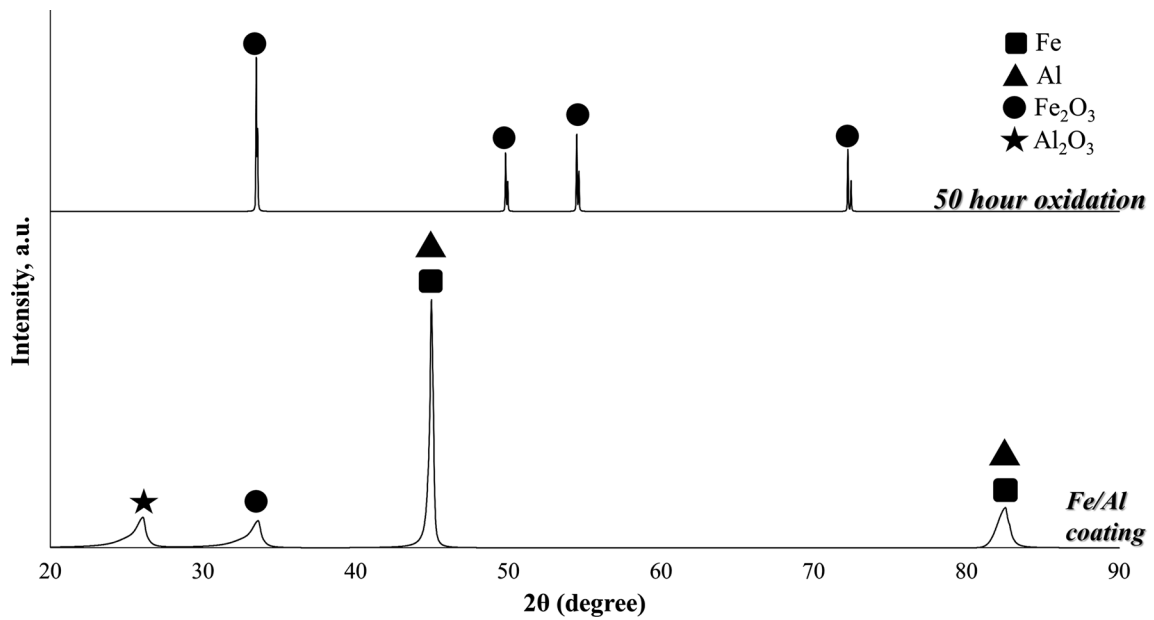


Fig. 7 XRD pattern of as-sprayed and 50-h oxidized Fe/Al coating

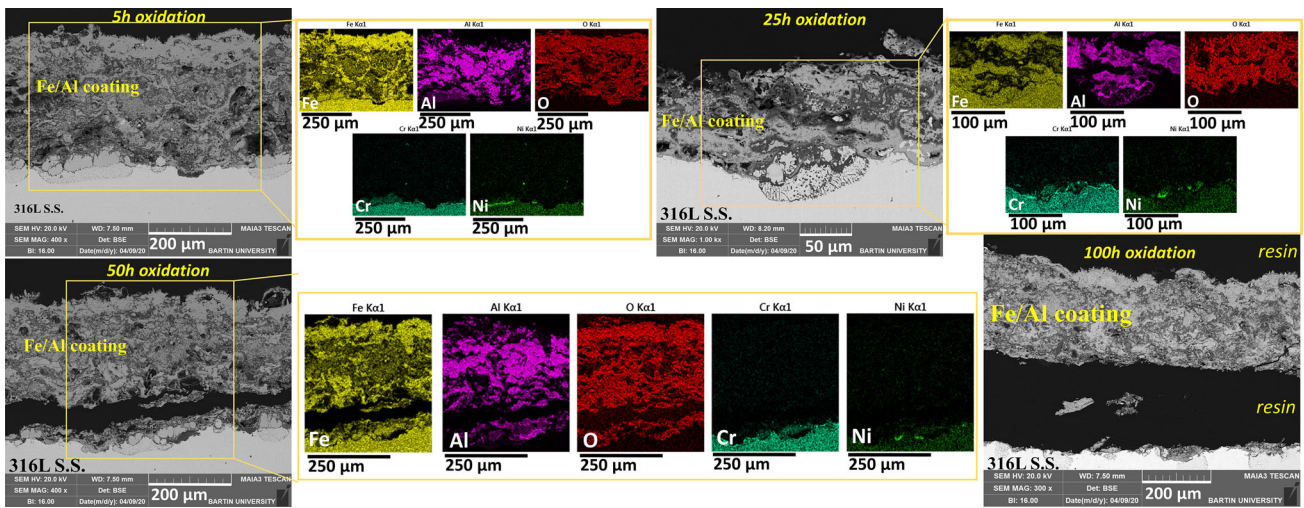


Fig. 8 SEM images of 5-, 25-, 50- and 100-h oxidized Fe/Al coating

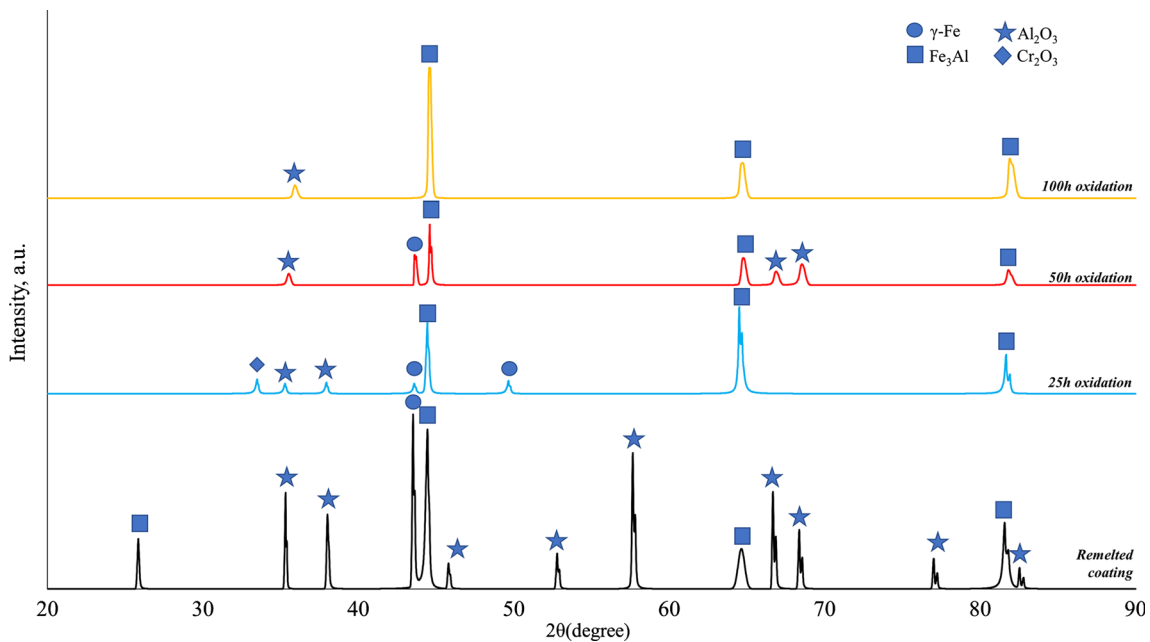


Fig. 9 XRD patterns belonging to as-remelted coating, 25-, 50- and 100-h oxidized remelted coating

After the oxidation tests, the changes in the oxide thickness are given in Fig. 12. The increase in the rate of the oxide thickness decreased with increased oxidation time in laser melted coating. According to Pilling and Bedworth's equation (Ref 26), when the square of mass change in the surface area ( $x$ ) versus oxidation time ( $t$ ) is plotted as a graph, the parabolic rate constant ( $k_p$ ) can be calculated using the slope of this plot. Similar to this approach, the thickness of the oxide layer ( $x$ ) can be used instead of the mass change in the surface area according to the formula.

$$x^2 = k_p \cdot t + C$$

where  $x$  is  $\mu\text{m}$ ,  $t$  is h,  $c$  is constant and  $k_p$  is  $\mu\text{m}^2/\text{h}$ . If the square of the oxide thickness versus the oxidation time is plotted as a graph, the parabolic rate constant can be calculated using the slope of this plot. The parabolic rate constant gives an idea about the growth rate of the oxide layer during the oxidation

tests. The obtained values can also be compared to each other to estimate the lifetime of the samples depending on oxide thickness. The parabolic rate constants of the oxidized substrate and oxidized remelted-coating were obtained by the slope of the square of the oxide thickness–oxidation time graph in Fig. 12. For the Fe/Al coating, the parabolic rate constant was not calculated because it was completely oxidized after the oxidation tests. When the  $k_p$  value of the substrate was calculated, the oxide thickness of the substrate was taken until 50 h due to the spallation of the oxide layer in 100-h oxidation test. The remelted coating has lower oxide thickness and  $k_p$  values compared to the substrate material as expected. The rate constant of 316L stainless steel and the remelted coating is found as 26.931 and 0.1638  $\mu\text{m}^2/\text{h}$  according to Fig. 12, respectively. The remelted Fe/Al coating seriously improved the oxidation performance of the substrate material when considering the obtained  $k_p$  values.



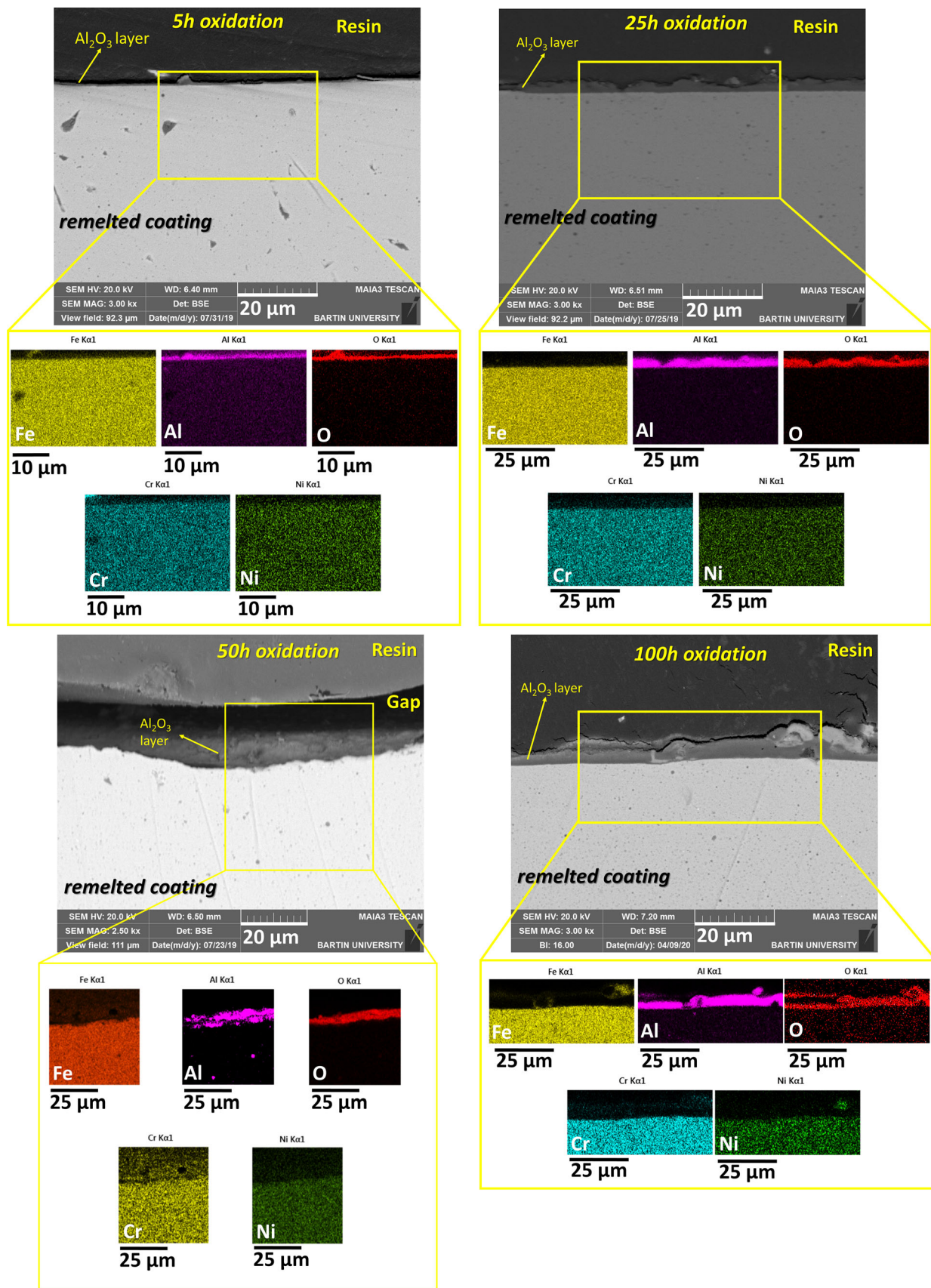


Fig. 10 SEM and elemental mapping images of 5-, 25-, 50- and 100-h oxidized remelted coating

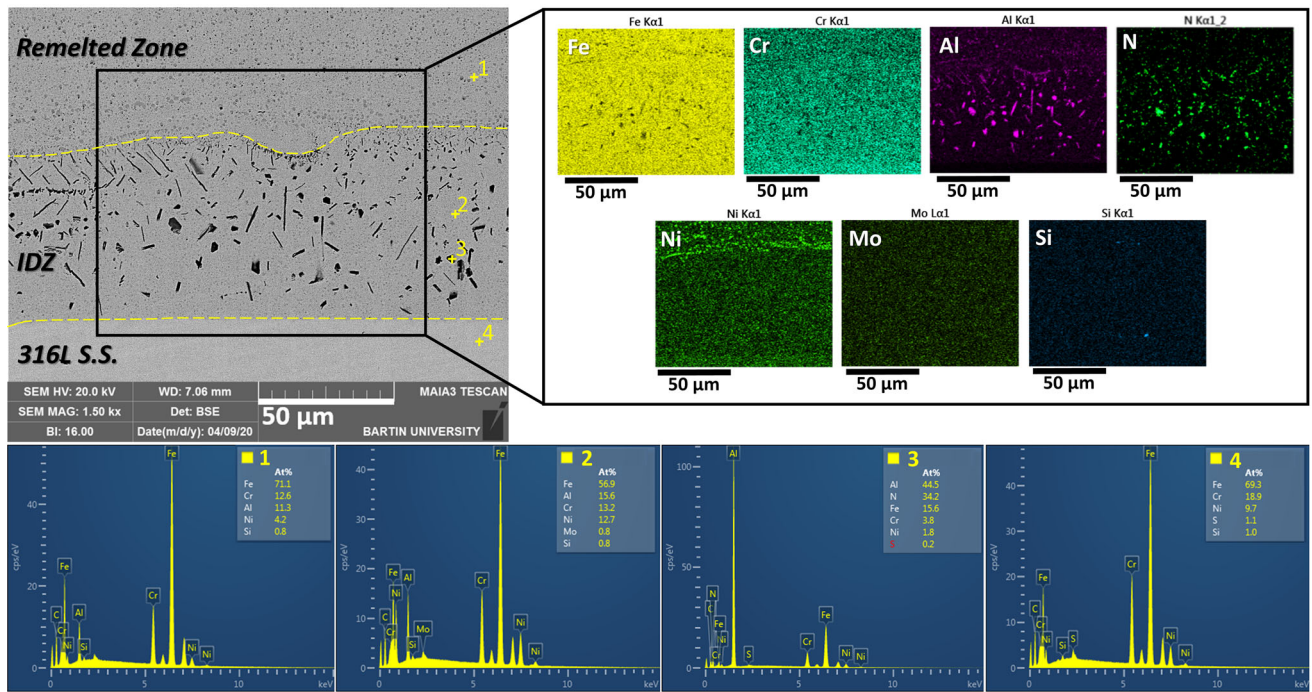


Fig. 11 Interface SEM, elemental point and mapping images of the substrate and the remelted coating at the end of the 100-h oxidation

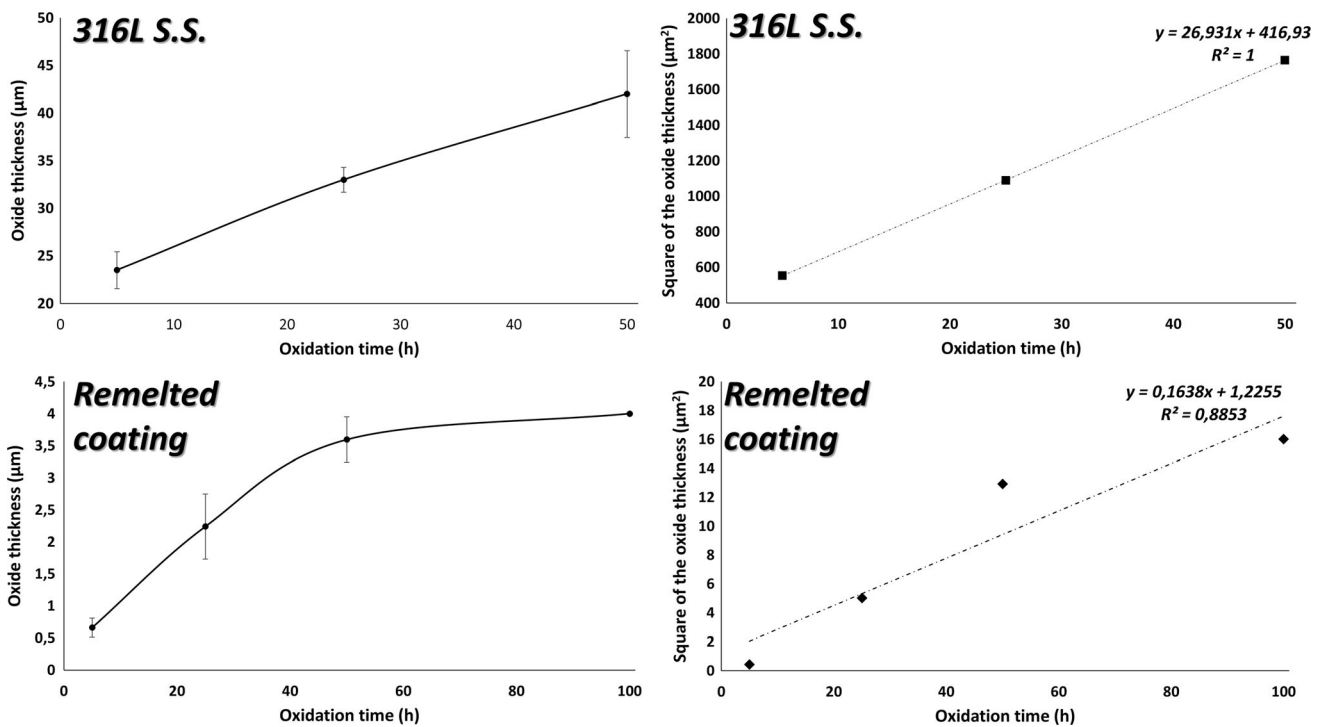


Fig. 12 Graphs of the oxide thickness and square of the oxide thickness versus oxidation time belonging to the substrate and remelted coating

It is well known that oxides with lower standard Gibbs free energy are highly stable. Oxidation occurs depending on the elemental affinity to oxygen. If the formed oxides have high stability, oxygen penetration proceeds slowly. According to standard Gibbs free energy after oxidation, when considering the elemental distribution of laser-remelted layer, first  $\text{Al}_2\text{O}_3$ , then  $\text{Cr}_2\text{O}_3$  and finally other oxides such as  $\text{Fe}_2\text{O}_3$ ,  $\text{NiO}$  and  $(\text{Fe}, \text{Ni})\text{Cr}_2\text{O}_4$  form. The reason for this is that Cr-O, Ni-O and

Al-O have phase diagrams that can be dissolved in each proportion, in both liquid and solid states. The initial oxidation stage is very important for a longer lifetime of alloys at high temperatures. In this stage, fast-growing oxides such as spinels can form and cause the earlier failure of the oxide layer (Ref 27). Using  $\text{CO}_2$  in the remelting process provided alumina formation prior to the oxidation tests. It is supposed that when Al content was depleted,  $\text{Cr}_2\text{O}_3$  and other oxides form,

respectively. The formation of other oxides is detrimental for the oxide layer. Thus, 316L stainless steel did not provide a continuous and stable oxide formation despite the high Cr content.

Alumina acts as a very well oxygen barrier for metallic components. The formation of the alumina layer is particularly desirable for metallic materials to provide protection against high-temperature oxidation. Thus, aluminide intermetallic materials are widely used at high temperatures. However, alloys with high Al content cannot be useful in some conditions due to the early spallation of the alumina layer. Some alloying elements suppress the metastable oxides and promote the nucleation of the stable oxide. It is known that Cr has an alumina-forming effect in alloys (Ref 28, 29). Alumina-forming austenitic (AFA) stainless steels are popular against high-temperature oxidation. Its composition range is close to that of the sample produced in this study instead of Nb (Ref 30). For instance, AFA 316 SS contains 3.482% aluminum as weight as well as Fe, Ni and Cr (Ref 31). Al has the highest affinity to oxygen among the elements present in this alloy. Under high-temperature condition, selectively oxidized Al forms  $\text{Al}_2\text{O}_3$  layer and it protects the alloy against oxidation. In this study, the same effect was obtained by the remelted Fe/Al coating. Another important effect of the alloying elements is the facilitated phase transformation of alumina ( $\gamma$ ,  $\delta$ ,  $\theta$ ,  $\alpha$ - $\text{Al}_2\text{O}_3$ ) (Ref 32, 33). Metastable fast-growing oxides lead to the early consumption of aluminum. It is known that void or cavity formation can occur below the oxide scale after the oxidation of aluminides such as FeAl and NiAl. Scale adherence was affected negatively by these formations (Ref 34). The consumption of the aluminum can lead to inward diffusion of Fe or Ni elements due to the concentration gradient. The presence of other elements plays a preventive role in the occurrence of this phenomenon. Cavity or void formation was not detected after the SEM examination in this study. Guilemany et al. (Ref 35) produced HVOF FeAl coating using gas atomized Fe-40Al-0.05Zr powders to investigate its high-temperature oxidation performance for 4, 36 and 72 h at 900 °C. After the oxidation tests, the oxide layer consists of  $\theta$ - $\text{Al}_2\text{O}_3$ ,  $\text{Fe}_2\text{O}_3$  and FeAl phases and there was no spallation or crack. In our study, no oxide phase other than alumina was detected and the observed alumina has alpha phase. The formation of  $\theta$ - $\text{Al}_2\text{O}_3$  in Fe-40Al was related to the transformation temperature of alumina. However, in the current study, remelting with  $\text{CO}_2$  provides a faster transformation of  $\alpha$ - $\text{Al}_2\text{O}_3$  which is more stable than other transition phases. The formation of early alumina is related to the low pressure. Similarly in another study (Ref 36), FeAl coatings were produced using magnetron sputtering and then oxidized at 1000 °C. The obtained results showed that  $\theta$ - $\text{Al}_2\text{O}_3$  formation caused higher mass gain in the initial stage of oxidation.

Xu et al. (Ref 37) investigated the isothermal oxidation behavior of Fe- $x$ Al ( $x = 10, 15$  and  $20$ , at.%) at 800 °C for 24 h. Alloys with 10 at.% and 15 at.% Al content formed a thin alumina layer and a thick  $\text{Fe}_2\text{O}_3$  layer, while Fe-20Al alloy consisted of a single alumina layer. This result causes higher oxide thickness and higher parabolic rate constant in alloys with low Al content. Compared with the current study, alumina was only formed as an oxide phase through the higher oxidation temperature. This result can be related to the Cr content of the substrate which facilitates the formation of alumina and the use of  $\text{CO}_2$  laser beam that leads to earlier alumina formation. Using another new production technique,

Fe- $x$ Al $_y$  coating was deposited on 316L stainless steel by high-energy micro-arc alloying technique which is a pulsed-arc micro-welding (Ref 38). The coatings can be produced in a very short time using this technique. After the oxidation tests, the formed alumina layer provides an excellent oxidation performance.

In the aluminizing process, porosity formation can be observed between the aluminide layer and the oxide layer due to the Kirkendall effect after oxidation (Ref 32). This formation causes early damage in the oxide layer. The same effect can also be seen between the aluminide layer and substrate material due to the different diffusion coefficient of elements after the homogenization heat treatment (Ref 39, 40).

In the high-temperature oxidation of iron aluminide materials, the coefficient of thermal expansion plays an important role in oxide scale spallations. Thermal expansion mismatch between metal and oxide layers leads to compressive stress which can result in oxide spallation. The increased Al ratio in FeCrAl alloy negatively affects the coefficient of thermal expansion (Ref 41). This causes early spallation of the alumina layer during the high-temperature oxidation process. The increased Al ratio causes the formation of intermetallic phases such as FeAl and  $\text{Fe}_3\text{Al}$  to higher extents. Alloys with rare earth element content may provide a lower Al consumption rate during the oxidation (Ref 41). In this study, the oxide scale spallation was not observed. It is supposed that the coating layer mainly consists of Fe-Cr-Ni-Al elements, and Al ratio is lower than the other elements. Thus, the thermal expansion mismatch between the alumina and coating layer may be lower than Fe-Al coatings.

The addition of rare earth elements has a positive effect on the oxidation performance of Al- and Cr-based alloy. Selective oxidation rate, cation grain boundary transport and scale adhesion can be enhanced with the addition of a minor amount of reactive element (Ref 42). Przybylski et al. (Ref 43) studied the effect of Zr addition on high-temperature oxidation behavior of  $\text{Fe}_3\text{Al}$ . Zr addition enhanced the oxidation resistance, provided better adhesion of the oxide scale and increased the oxygen diffusion along the grain boundary as tetragonal- $\text{ZrO}_2$  formations provide higher anionic diffusion along alumina grain boundaries. Similar to this study, Hotar et al. (Ref 44) investigated Zr addition on  $\text{Fe}_3\text{Al}$  alloy with respect to oxidation performance. Yet oxidation performance was negatively affected with the increased Zr content. The alloy with the lowest Zr content exhibited better performance. Similarly, Xu et al. (Ref 37) studied the addition of Y reactive element in Fe- $x$ Al ( $x = 10, 15$  and  $20$ , at.%) alloys to see its effect on the oxidation performance. Fe- $x$ Al alloys without Y show lower oxide growth at the end of the oxidation test. In the current study, the produced coatings do not involve a reactive element. It is supposed that the addition of a reactive element to Fe/Al composite can improve the alumina scale adherence and the coating can be more suitable for use at higher temperatures. However, it should be deeply investigated.

## 4. Conclusion

In the present study, 316 L stainless steel substrate and remelted Fe/Al coating were subjected to the isothermal oxidation tests. The obtained results were summarized as below:

1. Composite Fe/Al powders were sprayed on 316L stainless steel substrate using the HVOLF technique and then successfully remelted by the CO<sub>2</sub> laser beam. The coating layer with Fe-Cr-Ni-Al content and very thin alumina layer were obtained in a cheap and fast way.
2. The hardness values of Fe/Al coating were significantly improved with the remelting process.
3. 316L stainless steel and Fe/Al coating were affected by the high-temperature oxidation. The formed oxide scale was significantly thickened due to the formed iron oxides and spinel phases; in addition to this, crack formations induced by oxidation were observed.
4. Fe/Al coating is completely oxidized, and initiation of spallation and delamination was observed after 25-h oxidation tests. A protective oxide scale was not observed at the end of the oxidation tests.
5. Laser-remelted coating consisted of a thin alumina layer at the end of the oxidation tests. The presence of a compact alumina layer provided better oxidation performance. The formed oxide layers did not spall or crack. The low Al content in the remelted coating provides an advantage in terms of thermal expansion mismatch. An effect similar to AFA steels was obtained on the surface.
6. AlN phases were observed in IDZ after the oxidation tests. IDZ causes poor Al in the remelted zone due to the formation of AlN phases. However, it does not show a serious effect on the oxidation performance of the remelted coating.

As a result, laser-remelted Fe/Al coating improves both the hardness and oxidation resistance compared to the substrate and HVOLF Fe/Al coating. In future studies, the wear behavior of remelted Fe/Al coating and effect of the addition of minor amounts of reactive elements in laser-remelted Fe/Al composite coatings and its effect on the hot corrosion and oxidation performance of the coatings will be investigated.

## References

1. M.R. Dorfman, Thermal Spray Coatings, *Handbook of Environmental Degradation of Materials*, M. Kutz, Ed., William Andrew Publishing, 2005, p 405–422
2. L. Pawlowski, *The Science and Engineering of Thermal Spray Coatings*, 2nd ed., Wiley, New York, 2008
3. H. Singh, M.S. Grewal, H.S. Sekhon, and R.G. Rao, Sliding Wear Performance of High-Velocity Oxy-Fuel Spray Al<sub>2</sub>O<sub>3</sub>/TiO<sub>2</sub> and Cr<sub>2</sub>O<sub>3</sub> Coatings, *Proc. Inst. Mech. Eng. Part J J. Eng. Tribol.*, 2008, **222**(4), p 601–610. <https://doi.org/10.1243/13506501jet362>
4. M.E. Aalamiaieagha, S.J. Harris, and M. Emamighomi, Influence of the HVOF Spraying Process on the Microstructure and Corrosion Behaviour of Ni-20%Cr Coatings, *J. Mater. Sci.*, 2003, **38**(22), p 4587–4596
5. T. Sudaprasert, P.H. Shipway, and D.G. McCartney, Sliding Wear Behaviour of HVOF Sprayed WC-Co Coatings Deposited with Both Gas-Fuelled and Liquid-Fuelled Systems, *Wear*, 2003, **255**(7-12), p 943–949
6. J.A. Cabral-Miramontes, C. Gaona-Tiburcio, F. Almeraya-Calderón, F.H. Estupiñan-Lopez, G.K. Pedraza-Basulto, and C.A. Poblano-Salas, Parameter Studies on High-Velocity Oxy-Fuel Spraying of CoNiCrAlY Coatings Used in the Aeronautical Industry, *Int. J. Corros.*, 2014, **2014**, p 1–8
7. B. Song, M. Bai, K.T. Voisey, and T. Hussain, Role of Oxides and Porosity on High-Temperature Oxidation Of Liquid-Fueled HVOF Thermal-Sprayed Ni50Cr Coatings, *J. Therm. Spray Technol.*, 2017, **26**, p 554–568
8. M. Vostrák, M. Hruška, and Š. Houdková, Laser Re-melting of HVOF Sprayed NiCrBSi Coatings, in *METAL 2013—22nd International Conference on Metallurgy and Materials, Conference Proceedings* (2013) pp. 921–925
9. I.D. Utu and G. Marginean, Effect of Electron Beam Remelting on the Characteristics of HVOF sprayed Al<sub>2</sub>O<sub>3</sub>-TiO<sub>2</sub> Coatings Deposited on Titanium Substrate, *Colloids Surf. A Physicochem. Eng. Asp.*, 2017, **526**, p 70–75
10. M. Afzal, M. Ajmal, A. Nusair Khan, A. Hussain, and R. Akhter, Surface Modification of Air Plasma Spraying WC-12%Co Cermet Coating by Laser Melting Technique, *Opt. Laser Technol.*, 2014, **56**, p 202–206
11. E. Yasa, J. Deckers, and J.P. Kruth, The Investigation of the Influence of Laser Re-melting on Density, Surface Quality and Microstructure of Selective Laser Melting Parts, *Rapid Prototyp. J.*, 2011, **17**(5), p 312–327
12. R. González, M. Cadenas, R. Fernández, J.L. Cortizo, and E. Rodríguez, Wear Behaviour of Flame Sprayed NiCrBSi Coating Remelted by Flame or by Laser, *Wear*, 2007, **262**(3-4), p 301–307
13. Z. Brytan, M. Bonek, L.A. Dobrzański, D. Ugues, and M.A. Grande, The Laser Surface Remelting of Austenitic Stainless Steel, *Mater. Sci. Forum*, 2010, **654–656**, p 2511–2514
14. Q. Han and Y. Jiao, Effect of Heat Treatment and Laser Surface Remelting on AlSi10Mg Alloy Fabricated by Selective Laser Melting, *Int. J. Adv. Manuf. Technol.*, 2019, **102**(9-12), p 3315–3324. <https://doi.org/10.1007/s00170-018-03272-y>
15. Z. Wang, Q. Zhang, P. Guo, X. Gao, L. Yang, and Z. Song, Effects of Laser Surface Remelting on Microstructure and Properties of Biodegradable Zn-Zr Alloy, *Mater. Lett.*, 2018, **226**, p 52–54
16. M. Rakhes, E. Koroleva, and Z. Liu, Improvement of Corrosion Performance of HVOF MMC Coatings by Laser Surface Treatment, *Surf. Eng.*, 2011, **27**(10), p 729–733. <https://doi.org/10.1179/1743294411Y.0000000001>
17. H.T. Wang, C.J. Li, G.J. Yang, and C.X. Li, Effect of Heat Treatment on the Microstructure and Property of Cold-Sprayed Nanostructured FeAl/Al<sub>2</sub>O<sub>3</sub> Intermetallic Composite Coating, *Vacuum*, 2008, **83**(1), p 146–152
18. C. Senderowski, Nanocomposite Fe-Al Intermetallic Coating Obtained by Gas Detonation Spraying of Milled Self-Decomposing Powder, *J. Therm. Spray Technol.*, 2014, **23**(7), p 1124–1134
19. T. Chmielewski, P. Siwek, M. Chmielewski, A. Piątkowska, A. Grabias, and D. Golański, Structure and Selected Properties of Arc Sprayed Coatings Containing In-situ Fabricated Fe-Al Intermetallic Phases, *Metals (Basel)*, 2018, **8**(12), p 1059. <https://doi.org/10.3390/met8121059>
20. Q. Zhang, C.J. Li, X.R. Wang, Z.L. Ren, C.X. Li, and G.J. Yang, Formation of NiAl Intermetallic Compound by Cold Spraying of Ball-Milled Ni/Al Alloy Powder Through Postannealing Treatment, *J. Therm. Spray Technol.*, 2008, **17**, p 715–720
21. H.Y. Lee, S.H. Jung, S.Y. Lee, and K.H. Ko, Fabrication of Cold Sprayed Al-Intermetallic Compounds Coatings by Post Annealing, *Mater. Sci. Eng. A*, 2006, **433**(1-2), p 139–143
22. H.T. Wang, C.J. Li, G.J. Yang, and C.X. Li, Cold Spraying of Fe/Al Powder Mixture: Coating Characteristics and Influence of Heat Treatment on the Phase Structure, *Appl. Surf. Sci.*, 2008, **255**(5 PART 1), p 2538–2544
23. T. Chmielewski and D.A. Golański, New Method of In-situ Fabrication of Protective Coatings Based on Fe-Al Intermetallic Compounds, *Proc. Inst. Mech. Eng. Part B J. Eng. Manuf.*, 2011, <https://doi.org/10.1177/2041297510394050>
24. H. Buscail, R. Rolland, and S. Perrier, Cyclic Oxidation of AISI, 316L Stainless Steel—Influence of Water Vapour Between 800 and 1000 °C, *Corros. Eng. Sci. Technol.*, 2014, **49**(3), p 169–179. <https://doi.org/10.1179/1743278213y.0000000111>
25. Y.Z. Liu, X.B. Hu, S.J. Zheng, Y.L. Zhu, H. Wei, and X.L. Ma, Microstructural Evolution of the Interface Between NiCrAlY Coating and Superalloy During Isothermal Oxidation, *Mater. Des.*, 2015, **2015**(80), p 63–69
26. N. Pilling and R. Bedworth, The Oxidation of Metals at High Temperatures, *J. Inst. Met.*, 1923, **29**, p 529
27. M. Daroonparvar, M.A.M. Yajid, N.M. Yusof, M.S. Hussain, and H.R.B. Rad, Formation of a Dense and Continuous Al<sub>2</sub>O<sub>3</sub> Layer in nano thermal barrier coating systems for the Suppression of Spinel

- Growth on the Al<sub>2</sub>O<sub>3</sub> Oxide Scale During Oxidation, *J. Alloys Compd.*, 2013, **571**, p 205–220
28. K. Messaoudi, A.M. Huntz, and B. Lesage, Diffusion and Growth Mechanism of Al<sub>2</sub>O<sub>3</sub> Scales on Ferritic Fe-Cr-Al Alloys, *Mater. Sci. Eng. A*, 1998, **247**(1-2), p 248–262
  29. M.P. Brady, Y. Yamamoto, M.L. Santella, and B.A. Pint, Effects of Minor Alloy Additions and Oxidation Temperature on Protective Alumina Scale Formation in Creep-Resistant Austenitic Stainless Steels, *Scr. Mater.*, 2007, **57**(12), p 1117–1120
  30. M.P. Brady, J. Magee, Y. Yamamoto, D. Helmick, and L. Wang, Co-Optimization of Wrought Alumina-Forming Austenitic Stainless Steel Composition Ranges for High-Temperature Creep and Oxidation/Corrosion Resistance, *Mater. Sci. Eng. A*, 2014, **590**, p 101–115
  31. X. Guo, K. Chen, W. Gao, Z. Shen, and L. Zhang, Corrosion Behavior of Alumina-Forming and Oxide Dispersion Strengthened Austenitic 316 Stainless Steel in Supercritical Water, *Corros. Sci.*, 2018, **138**, p 297–306
  32. T. Yener, K.M. Doleker, and A. Erdogan, High Temperature Oxidation Behavior of Low Temperature Aluminized Mirrax<sup>®</sup> ESR Steel, *Mater. Res. Express*, 2019, **6**, p 116407
  33. K.M. Doleker, Y. Ozgurluk, H. Ahlatci, and A.C. Karaoglanli, Evaluation of Oxidation and Thermal Cyclic Behavior of YSZ, Gd<sub>2</sub>Zr<sub>2</sub>O<sub>7</sub> and YSZ/Gd<sub>2</sub>Zr<sub>2</sub>O<sub>7</sub> TBCs, *Surf. Coat. Technol.*, 2019, **371**, p 262–275. <https://doi.org/10.1016/j.surfcoat.2018.11.055>
  34. H.J. Grabke, Oxidation of NiAl and FeAl, *Intermetallics*, 1999, **7**(10), p 1153–1158
  35. J.M. Guilemany, N. Cinca, S. Dosta, and C.R.C. Lima, High-Temperature Oxidation of Fe<sub>40</sub>Al Coatings Obtained by HVOF Thermal Spray, *Intermetallics*, 2007, **15**(10), p 1384–1394
  36. Z. Liu, W. Gao, and F. Wang, Oxidation Behaviour of FeAl Intermetallic Coatings Produced by Magnetron Sputter Deposition, *Scr. Mater.*, 1998, **39**(11), p 1497–1502. [https://doi.org/10.1016/S1359-6462\(98\)00360-1](https://doi.org/10.1016/S1359-6462(98)00360-1)
  37. X. Xu, H. Wei, J. Xiang, L. Wang, M. Liu, H. Zhang, D. Men, and J. An, Oxidation Mechanism of Three Fe-Al Alloys with and Without Addition of 0.1 At% Y at 800 °C, *J. Rare Earths* (2019). <https://doi.org/10.1016/j.jre.2019.10.007>
  38. P. Guo, Y. Shao, C. Zeng, M. Wu, and W. Li, Oxidation Characterization of FeAl Coated 316 Stainless Steel Interconnects by High-Energy Micro-Arc Alloying Technique for SOFC, *Mater. Lett.*, 2011, **65**(19-20), p 3180–3183
  39. A.M. Hodge and D.C. Dunand, Synthesis of Nickel-Aluminide Foams by Pack-Aluminization of Nickel Foams, *Intermetallics*, 2001, **9**(7), p 581–589
  40. E. Huttunen-Saarivirta, F.H. Stott, V. Rohr, and M. Schütze, Erosion-Oxidation Behaviour of Pack-Aluminized 9% Chromium Steel Under Fluidized-Bed Conditions at Elevated Temperature, *Corros. Sci.*, 2007, **49**(7), p 2844–2865
  41. B.A. Pint, W.D. Porter, and I.G. Wright, The Effect of Thermal Expansion on Spallation Behavior of Fe-Base Alumina-Forming Alloys, *Mater. Sci. Forum*, 2008, **595–598**, p 1083–1092
  42. P.Y. Hou, The Reactive Element Effect—Past, Present and Future, *Mater. Sci. Forum*, 2011, **696**, p 39–44
  43. K. Przybylski, S. Chevalier, P. Juzoń, A. Galerie, G. Borchardt, O. Heintz, and J.P. Larpin, The Role of Zr in the High-Temperature Oxidation of Fe<sub>3</sub>Al, *Mater. Sci. Forum*, 2008, **595–598**, p 1103–1110
  44. A. Hotař, P. Kejzlar, M. Palm, and J. Mlnařik, The Effect of Zr on High-Temperature Oxidation Behaviour of Fe<sub>3</sub>Al-Based Alloys, *Corros. Sci.*, 2015, **100**, p 147–157

**Publisher's Note** Springer Nature remains neutral with regard to jurisdictional claims in published maps and institutional affiliations.